

ARTICLE

Open Access

# Probing the weak limit of magnetocrystalline anisotropy through a spin–flop transition in the van der Waals antiferromagnet CrPS<sub>4</sub>

Jae Yeon Seo<sup>1</sup>, Sunghyun Lim<sup>1</sup>, Hyun Jun Shin<sup>1</sup> , Ki Won Jeong<sup>1</sup>, Jae Min Hong<sup>1</sup>, Kyungsun Moon<sup>1</sup> ,  
Mi Kyung Kim<sup>1</sup> , Nara Lee<sup>1</sup>  and Young Jai Choi<sup>1</sup> 

## Abstract

The influence of magnetocrystalline anisotropy (MCA) on antiferromagnetism is elucidated through the characterization of the spin–flop transition. However, due to a lack of suitable candidates for investigation, a detailed understanding of the preservation of the spin–flop transition in the presence of low MCA energy remains elusive. In this study, we introduce CrPS<sub>4</sub>, which is a two-dimensional van der Waals antiferromagnet, as an ideal system to explore the exceedingly weak limit of the thermally-evolved MCA energy. By employing a uniaxially anisotropic spin model and fitting it to the experimental magnetic properties, we quantify the MCA energy and identify the discernible spin configurations in different magnetic phases. Notably, even at the limit of extremely weak MCA, with a mere 0.12% of the interlayer antiferromagnetic exchange interaction at  $T = 33$  K, which is slightly below the Néel temperature ( $T_N$ ) of 38 K, the spin–flop transition remains intact. We further establish a direct correlation between the visualized spin arrangements and the progressive reversal of magnetic torque induced by rotating magnetic fields. This analysis reveals the essential role of MCA in antiferromagnetism, thus extending our understanding to previously undetected limits and providing valuable insights for the development of spin-processing functionalities based on van der Waals magnets.

## Introduction

Two-dimensional (2D) van der Waals (vdW) magnets are composed of elemental magnetic multilayers and provide a unique platform for studying the fundamental aspects of magnetism in terms of reduced dimensionality and a favorable foundation for attaining atomically thin spin-processing functionalities<sup>1–9</sup>. At finite temperatures, the long-range magnetic order is in principle prohibited in 2D isotropic magnets without the presence of magnetocrystalline anisotropy (MCA), which breaks the ideal Heisenberg symmetry<sup>10</sup>. The intrinsic MCA, induced by a sizable spin-orbit interaction, plays a crucial role in preserving the magnetic order and preventing random spin

orientations driven by thermal fluctuations<sup>11–14</sup>. Furthermore, indirect exchange interactions between the 2D magnetic layers can be facilitated through the vdW gap<sup>15–18</sup>. Consequently, significant efforts have been dedicated toward enhancing and controlling anisotropy to improve the magnetization stability for various spintronic device applications, especially at higher temperatures<sup>14,19,20</sup>. Therefore, understanding the intimate connection between the magnetic order and MCA provides a fundamental basis for investigating diverse 2D magnetic characteristics.

The spin–flop transition is a field-induced spin reorientation phenomenon and occasionally observed in antiferromagnets. Because this causes significant changes in magnetically anisotropic properties through a phase conversion, the characterization of the spin–flop transition provides valuable insights into the impact of MCA on antiferromagnetism<sup>21–24</sup>. The MCA energies in vdW

Correspondence: Mi Kyung Kim ([kkummi.mi@yonsei.ac.kr](mailto:kkummi.mi@yonsei.ac.kr)) or Nara Lee ([eland@yonsei.ac.kr](mailto:eland@yonsei.ac.kr)) or Young Jai Choi ([phylove@yonsei.ac.kr](mailto:phylove@yonsei.ac.kr))

<sup>1</sup>Department of Physics, Yonsei University, Seoul 03722, Korea

These authors contributed equally: Jae Yeon Seo, Sunghyun Lim, Hyun Jun Shin

© The Author(s) 2024



**Open Access** This article is licensed under a Creative Commons Attribution 4.0 International License, which permits use, sharing, adaptation, distribution and reproduction in any medium or format, as long as you give appropriate credit to the original author(s) and the source, provide a link to the Creative Commons licence, and indicate if changes were made. The images or other third party material in this article are included in the article's Creative Commons licence, unless indicated otherwise in a credit line to the material. If material is not included in the article's Creative Commons licence and your intended use is not permitted by statutory regulation or exceeds the permitted use, you will need to obtain permission directly from the copyright holder. To view a copy of this licence, visit <http://creativecommons.org/licenses/by/4.0/>.

antiferromagnets have been theoretically estimated to be in the sub-meV range, which is comparable to the typical magnitude of antiferromagnetic exchange interactions<sup>25–27</sup>. However, investigating the spin–flop transition in the presence of weak MCA energy has proven challenging mainly due to the lack of suitable candidate materials for these investigations. vdW antiferromagnets MPS<sub>3</sub> (M: Fe, Ni, and Mn) exhibit antiferromagnetic order in the Néel (MnPS<sub>3</sub>) or zigzag types (FePS<sub>3</sub> and NiPS<sub>3</sub>) configurations<sup>28,29</sup>. These spin arrangements result from intralayer antiferromagnetic couplings, typically characterized by strong exchange interactions that lead to high spin–flop fields. For instance, the spin–flop transition in FePS<sub>3</sub> occurs above 35 T with pronounced magnetic hysteresis at  $T = 4$  K<sup>30</sup>; thus, it is unsuitable for investigating the weak limit of MCA.

In this study, we focus on the vdW interlayer antiferromagnet CrPS<sub>4</sub> to investigate the weak limit of thermally evolved MCA energy. The spin–flop transition could be sustained up to  $T = 33$  K, just below  $T_N$ , and this was verified through the presence of a pronounced peak in the magnetic torque measurements. By adopting the easy-axis spin model, we could estimate the MCA energy, which was only 0.12% of the interlayer antiferromagnetic exchange interaction. Furthermore, we established various spin textures in the presence of rotating magnetic fields, and these spin textures were strongly correlated with the angular dependence of magnetic torque data. This research highlights the essential role of MCA in antiferromagnetism and extends our understanding to previously undetected limits. The results contribute to the expanding field of 2D magnetism and its potential applications in spintronics and other emerging technologies.

## Materials and methods

### Crystal growth

Plate-like single crystals of CrPS<sub>4</sub> were synthesized using the chemical vapor transport method with iodine as the chemical agent<sup>31–33</sup>. Stoichiometric ratios of Cr, P, and S powders (1:1:4) were thoroughly mixed. The mixture was then placed at one end of a quartz tube, which was subsequently vacuum-sealed and loaded into a horizontal two-zone furnace. The hot zone of the furnace was maintained at 680 °C, while the cold zone was kept at 600 °C for one week. Then, the furnace was turned off and allowed to cool to room temperature. Shiny crystals a few millimeters in length formed in the cold zone of the quartz tube. Any residual iodine on the crystal surfaces was removed by washing with ethanol.

### Scanning transmission electron microscopy (STEM)

The CrPS<sub>4</sub> crystals used for the STEM measurements were carefully prepared based on a cutting plane perpendicular to the *b* axis using a dual-beam focused ion beam

system (Helios 650, FEI). To ensure minimal specimen damage, the acceleration voltage conditions were progressively reduced from 30 to 2 keV. Dark-field images were acquired using a STEM (JEM-ARM200F, JEOL Ltd., Japan) operating at 200 keV with a Cs-corrector (CESCOR, CEOS GmbH, Germany) and a cold field emission gun. During scanning, an electron probe with a size of 83 pm was employed, and the high-angle annular dark-field detector angle was varied within the range of 90–370 mrad.

### Magnetic property measurements

The magnetic susceptibility and isothermal magnetization measurements were performed using a vibrating sample magnetometer option in a physical property measurement system (PPMS, Quantum Design, Inc.). The measurements were conducted at temperatures in the range of  $T = 2$ –200 K with magnetic fields applied along the *b* and *c* axes of the crystals in the range of  $H = -9$ –9 T. To measure the magnetic torque depending on the magnetic field and angular orientation, a calibrated cantilever chip (P109A, Quantum Design, Inc.) was attached to a single-axis rotator in the PPMS. The magnetic torque is measured under the condition of an exceptionally low noise level ( $1 \times 10^{-9}$  N·m), with a Wheatstone bridge circuit to the cantilever chip.

### Easy-axis anisotropic spin Hamiltonian

The spin Hamiltonian for the A-type antiferromagnetic order of CrPS<sub>4</sub> is given by the following:

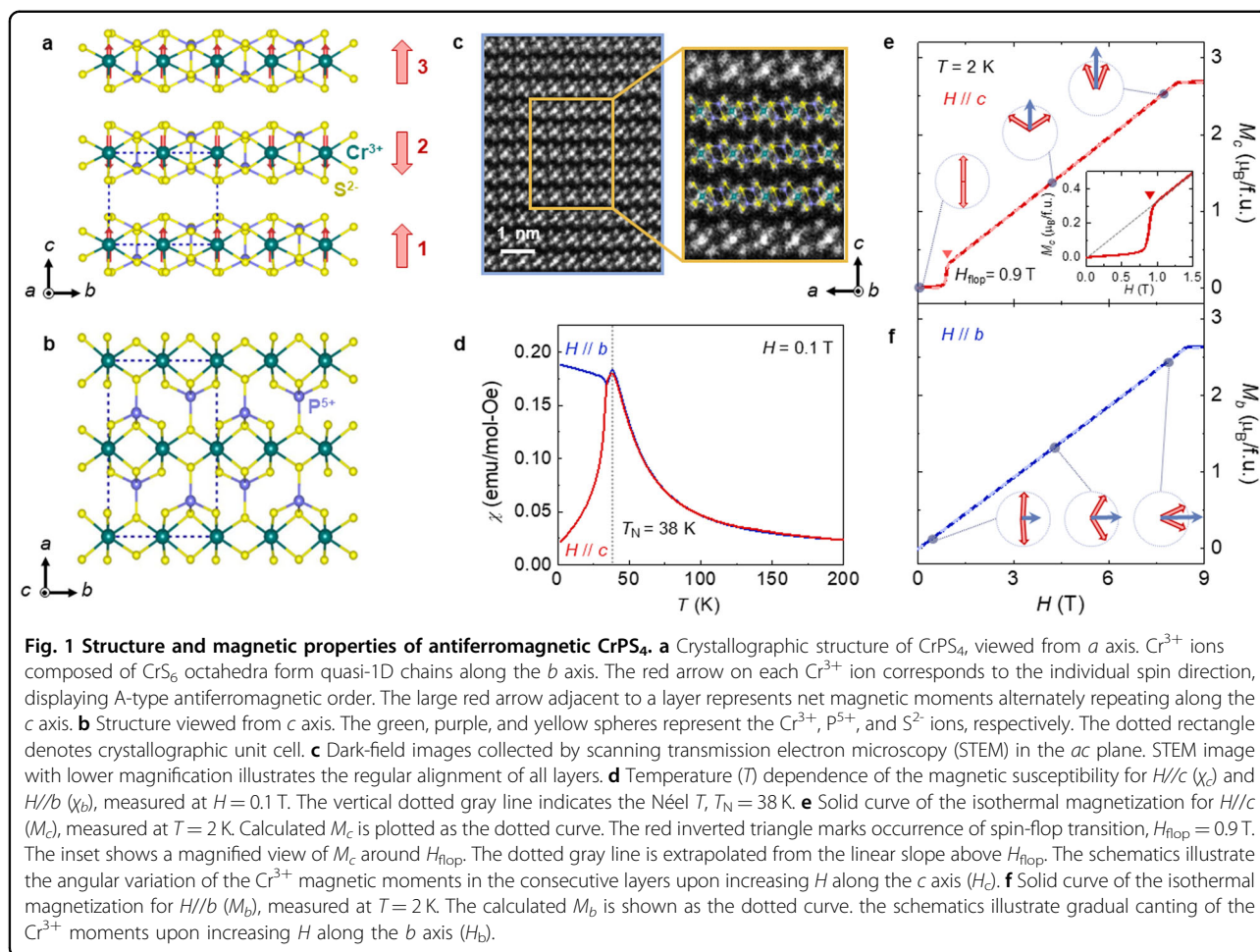
$$\mathcal{H}/N = J \sum_{i=1}^2 \vec{S}_i \cdot \vec{S}_{i+1} - g\mu_B \vec{H} \cdot \sum_{i=1}^2 \vec{S}_i + K \sum_{i=1}^2 \sin^2 \theta_i,$$

where  $N$  denotes the number of Cr<sup>3+</sup> moments in a single layer,  $\vec{S}_i$  is the Cr<sup>3+</sup> moment in the *i*-th layer,  $g = 2$ , and  $\mu_B$  is the Bohr magneton. The first term corresponds to the antiferromagnetic interactions, where  $J$  denotes the coupling strength ( $J > 0$ ) between the Cr<sup>3+</sup> moments in two neighboring layers. The system exhibits a pattern of alternating net magnetic moments along the *c* axis due to interlayer antiferromagnetic exchange interactions, as shown in Fig. 1a. Employing a periodic boundary condition with the summation of *i* up to 2 ensures sufficient accuracy, considering the identical nature of the 3rd and 1st moments. The second term denotes the Zeeman energy. The third term reflects the easy *c*-axis MCA, and here,  $K$  is the MCA energy. The angle  $\theta_i$  is the polar angle of the Cr<sup>3+</sup> moment in the *i*-th layer on the *bc* plane ( $\theta_i = 0^\circ$  for the *c*-axis and  $\theta_i = 90^\circ$  for the *b*-axis).

## Results

### Anisotropic magnetic properties and theoretical fittings

CrPS<sub>4</sub> exhibits a monoclinic crystal structure belonging to the  $C_2$  space group, with lattice constants  $a = 1.086$  nm,



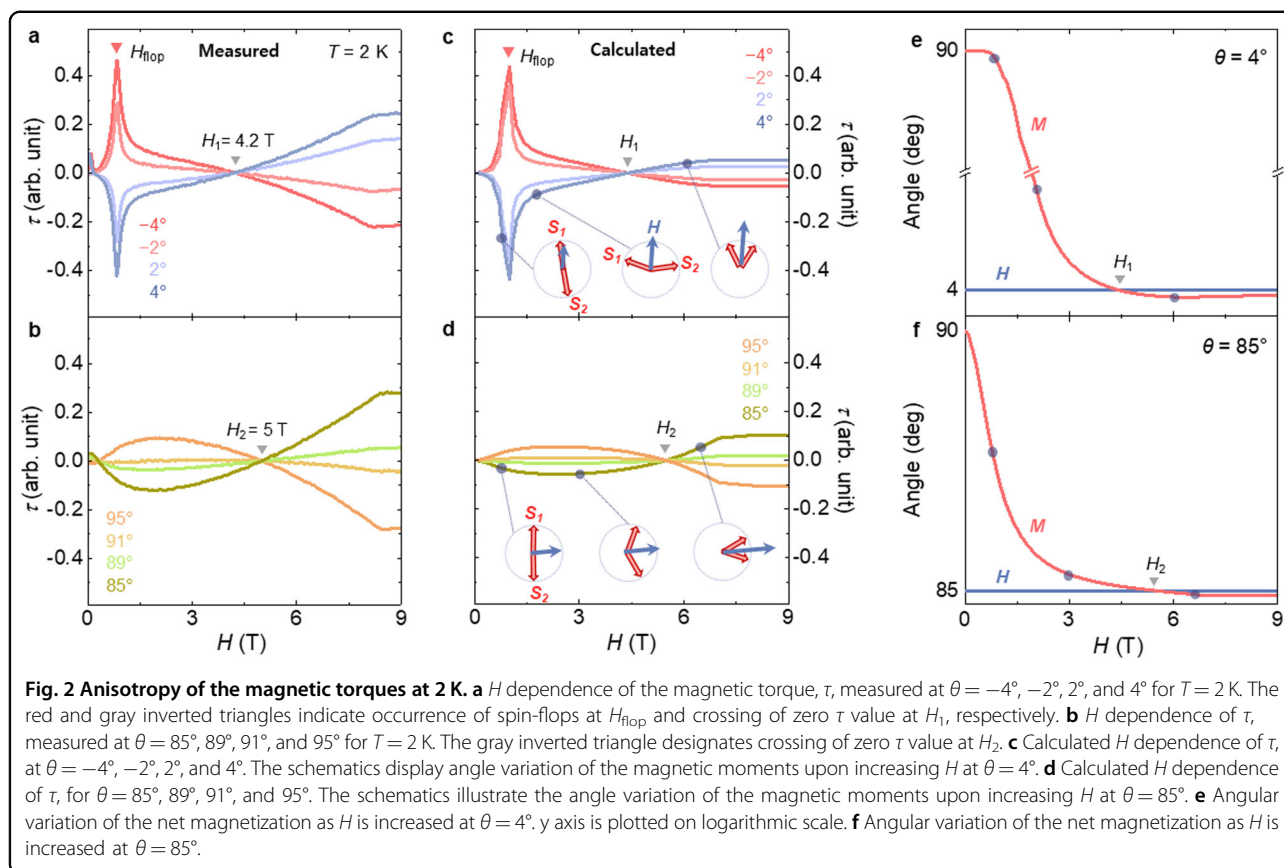
$b = 0.725$  nm,  $c = 0.614$  nm, and  $\beta = 91.88^\circ$ <sup>31</sup>. Each chromium ion (Cr<sup>3+</sup>,  $S = 3/2$ ) is coordinated by six sulfur ions (S<sup>2-</sup>), thus forming a slightly distorted CrS<sub>6</sub> octahedron, as depicted in Fig. 1a. These octahedra align along the *b* axis, thereby creating quasi-1D chains. Phosphorus ions (P<sup>5+</sup>) connect these chains, forming a 2D rectangular lattice, as shown in Fig. 1b. Close-packed S<sup>2-</sup> forms separate layers, resulting in significant vdW gaps, which facilitate easy exfoliation. This further leads to the formation of thin flakes or even monolayers<sup>34,35</sup>. The structural units are also visualized by STEM, and the vdW gaps that separate these units along the cutting plane are clearly resolved (Fig. 1c). X-ray diffraction was performed, and the distinct 112.5° arrangement of the Cr atoms within the *ab* plane (Supplementary Figs. S1 and S2) confirmed the crystallographic axes of the CrPS<sub>4</sub> crystals.

Recent studies employing powder neutron diffraction have confirmed that the magnetic Cr<sup>3+</sup> ions in CrPS<sub>4</sub> exhibit an A-type antiferromagnetic order<sup>12,31,36</sup>; this result is consistent with previous density functional theory calculations<sup>37</sup>. As shown in Fig. 1a, the net magnetic

moments of the adjacent layers of Cr<sup>3+</sup> ions are aligned in the opposite direction along the *c* axis, thus yielding a magnetic unit cell that is twice the size of the crystallographic unit cell. The Cr<sup>3+</sup> spins in the spin-flop state are known to lie in the *bc* plane, and this is associated with the presence of the quasi-1D chains of the CrS<sub>6</sub> octahedra along the *b* axis (Fig. 1a)<sup>31</sup>. Therefore, the magnetic properties were characterized by applying magnetic fields along the *c* axis (*H<sub>c</sub>*) and *b* axis (*H<sub>b</sub>*).

The magnetic susceptibility ( $\chi = M/H$ ) was measured at *H* = 0.1 T after zero-field cooling for orientations parallel to the *c* axis ( $\chi_c$ ) and *b* axis ( $\chi_b$ ) (Fig. 1d). Anomalies in both  $\chi_c$  and  $\chi_b$  indicate the onset of an antiferromagnetic order at a transition temperature (*T<sub>N</sub>*) of 38 K. *T<sub>N</sub>* was additionally estimated through molecular-field theory (see Supplementary S2). The high rate of decrease in  $\chi_c$  below *T<sub>N</sub>* is consistent with the A-type antiferromagnetic arrangement of Cr<sup>3+</sup> moments.

Isothermal magnetization (*M*) measurements at *T* = 2 K reveal the magnetically anisotropic behavior of CrPS<sub>4</sub>, as displayed in Figs. 1e, f. The slight linear slope of *M<sub>c</sub>* at low



$H_c$  values can be attributed to fractional flips of  $\text{Cr}^{3+}$  spins that were initially aligned in a direction opposite to that of  $H_c$ . A small but sudden increase at  $H_{\text{flop}} = 0.9$  T indicates a spin-flop transition, wherein the moments of  $\text{Cr}^{3+}$  ions are partially polarized, and this can be identified through the extrapolation of a linear slope above  $H_{\text{flop}}$  intersecting at the origin (inset of Fig. 1e)<sup>38,39</sup>. Furthermore, the increase in  $H_c$  induces additional canting of the flopped moments, which produces the saturated state at  $H_{\text{sat.}} \approx 8.1$  T. The schematics in Fig. 1e illustrate the evolution of the  $\text{Cr}^{3+}$  magnetic moments across the spin-flop transition. In contrast,  $M_b$  exhibits a linear increase due to the gradual canting of  $\text{Cr}^{3+}$  magnetic moments toward the  $H_b$  direction, and the magnetic moment saturates at approximately 8.4 T (Fig. 1f).

Despite the relatively large isotropic spin state within the octahedral environment of the  $\text{Cr}^{3+}$  ions, the slight preference for the  $\text{Cr}^{3+}$  moment orientation along the  $c$  axis and the occurrence of a small spin-flop transition at low  $H_c$  indicate the existence of a marginal MCA. To obtain further insights into the essential characteristics of the spin-flop transition within the context of a weak MCA, we employed an easy-axis anisotropic spin model, as described in the Methods section<sup>40,41</sup>. Based on a systematic analysis of the total magnetic energy as  $H_c$

increases, we conducted a precise fitting of the theoretical model to the experimental  $M_c$  at 2 K. This enabled the determination of the ratio between the exchange coupling ( $JS^2$ ) and Zeeman energy ( $g\mu_B HS$ ), yielding a value of  $g\mu_B H_{\text{flop}} S/JS^2 = 0.43$  and  $JS^2 = 0.24$  meV. Furthermore, we performed an additional fitting to the experimental  $M_b$  at 2 K, yielding a ratio between the MCA energy ( $K$ ) and  $JS^2$ ,  $K/JS^2 = 2.26\%$  with  $K = 0.0054$  meV. Notably, this result differed from  $K/JS^2 = 27.27\%$ , as estimated for another vdW A-type antiferromagnet,  $\text{MnBi}_2\text{Te}_4$  (see Supplementary Fig. S3).

### Probing spin-flop transition by magnetic torques

The measurement of magnetic torque per unit volume, denoted as  $\tau = \mathbf{M} \times \mathbf{H}$ , serves as an ideal approach to investigate the anisotropic magnetic properties and the occurrence of spin-flop transitions, as shown in Figs. 2a and 2b. The anisotropic signals in the  $H$ -dependent  $\tau$  were observed at angles  $\theta$  close to  $0^\circ$  and  $90^\circ$ , where  $\theta$  represents the deviation of  $H$  from the  $c$  axis ( $\theta = 0^\circ$  corresponds to the  $c$  axis, and  $\theta = 90^\circ$  corresponds to the  $b$  axis) (see Supplementary Fig. S4). In contrast to the small step observed in  $M_c$  at  $H_{\text{flop}}$ , the  $\tau$  at  $T = 2$  K and  $\theta = -2^\circ$  exhibits a distinct and sharper peak at  $H_{\text{flop}}$  (Fig. 2a). With a further increase in  $H$ ,  $\tau$  gradually decreases and changes

its sign at  $H_1 = 4.2$  T. The increase in the rotation of  $\theta$  to  $\theta = -4^\circ$  enhances the peak height at  $H_{\text{flop}}$ . By changing the sign of  $\theta$  that corresponds to the opposite angle between the net  $M$  and  $H$ ,  $\tau$  is fully reversed. Conversely, the  $\tau$  at angles close to  $90^\circ$  demonstrates a minor and broad variation as  $H$  increases, followed by a change in the negative values and crossing zero at  $H_2 = 5.0$  T (Fig. 2b). The anisotropic characteristics of CrPS<sub>4</sub> are evident in the behavior of  $\tau$  despite the relatively small value of the MCA energy.

By employing a uniaxial anisotropic spin Hamiltonian and explicitly estimating the net Cr<sup>3+</sup>-moment orientation relative to  $H$  in each layer, we successfully reproduced the anisotropic  $H$ -dependent  $\tau$  at angles  $\theta$  close to  $0^\circ$  and  $90^\circ$ , as illustrated in Figs. 2c and 2d. For  $\theta = 4^\circ$  and  $H$  below  $H_{\text{flop}}$ , the net Cr<sup>3+</sup> moment in the lower layer ( $S_2$  moment) is slightly canted due to the weak  $H_b$  component, while the net Cr<sup>3+</sup> moment in the upper layer ( $S_1$  moment) tends to align predominantly along the  $H_c$  direction (Fig. 2c). This larger rotation of the  $S_2$  moment results in an angle of net  $M$  below  $90^\circ$ , and this yields negative values of  $\tau$  (Fig. 2e). The relative angle between  $M$  and  $H$  gradually decreases up to  $H_{\text{flop}}$ , but  $\tau$  continues to increase due to the high rate of increase in  $H$ . When  $H$  surpasses  $H_{\text{flop}}$ , the angle of net  $M$  rapidly decreases but is larger than  $\theta = 4^\circ$ , thereby sustaining negative values of  $\tau$ . For  $H$  above  $H_1$ , the strong  $H_c$  component predominantly aligns the two net moments of both layers closer to the  $H_c$  direction. Since the influence of the  $H_b$  component on the moments is not significant, the angle of net  $M$  is situated below  $\theta = 4^\circ$ , causing a sign reversal in  $\tau$ . Under  $H$  for  $\theta = 85^\circ$ , the angle of net  $M$  becomes larger than  $\theta$  due to the configuration of the  $S_1$  moment (Figs. 2d and 2f). This arrangement causes the generation of negative values for  $\tau$ . At  $H$  greater than  $H_2$ , the  $H_c$  component causes the  $S_1$  moment to be less tilted toward the  $H_b$  direction, generating a change in the sign of  $\tau$  to positive values. The  $T$  development of anisotropic  $H$ -dependent  $\tau$  is shown in Supplementary Fig. S5.

### Weak limit of magnetocrystalline anisotropy

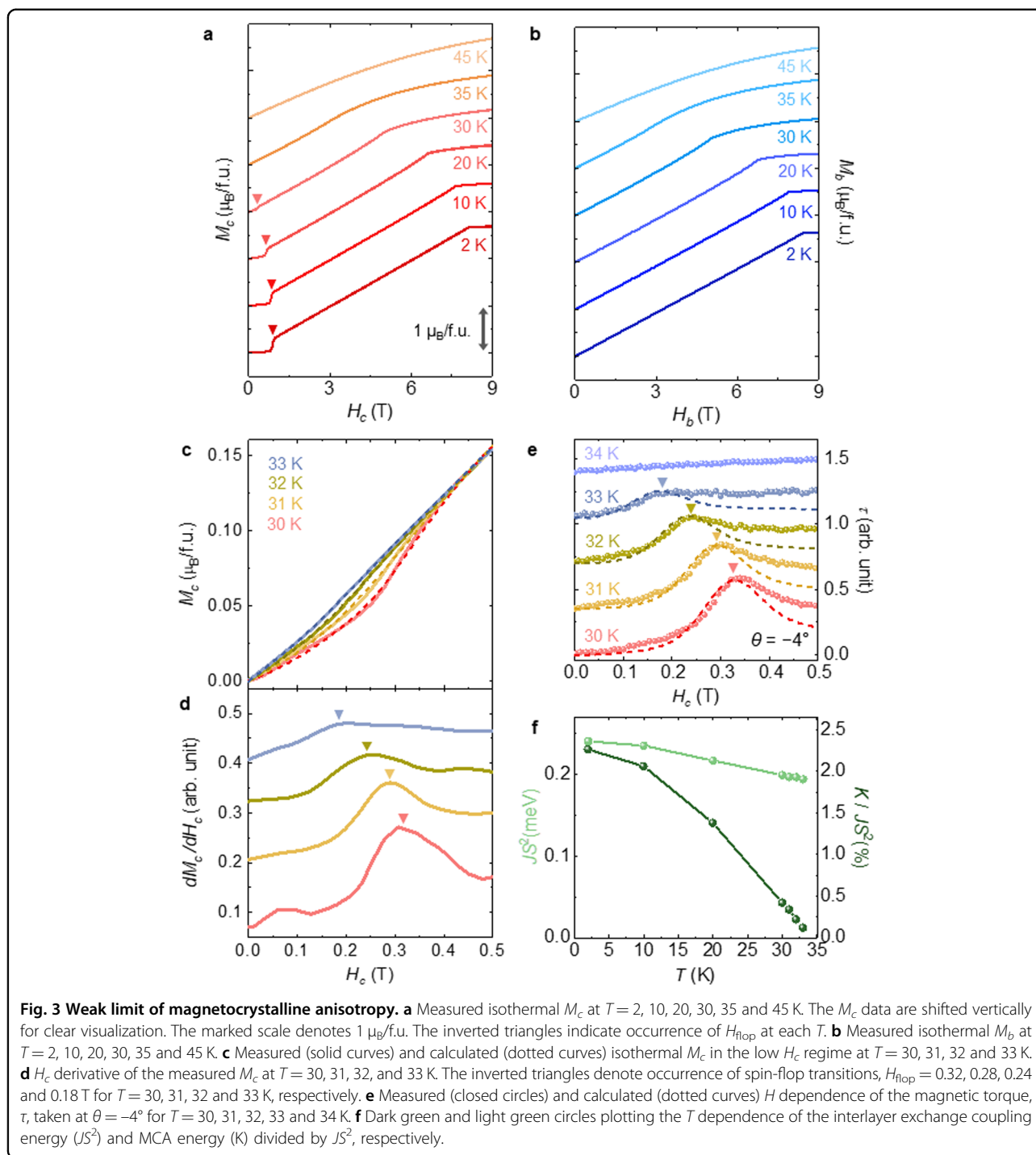
In the context of the anisotropic spin model, the magnetic energies of the spin-flop state and A-type antiferromagnetic state in CrPS<sub>4</sub> can be described as follows:  $E_{\text{flop}} = 2JS^2 \cos 2\theta - 2g\mu_B HS \cos \theta + 2Ks \sin^2 \theta$  and  $E_{\text{AFM}} = -2JS^2$ , respectively (see Supplementary Fig. S6). The optimal canting angle of the Cr<sup>3+</sup> moments in the spin-flop state,  $\cos \theta_{\text{flop}} = g\mu_B HS / 2(2JS^2 - K)$ , can be derived from  $\partial E_{\text{flop}} / \partial \theta = 0$ . Consequently, the condition that  $E_{\text{flop}}(\theta_{\text{flop}}) = E_{\text{AFM}}$  at  $H_{\text{flop}}$  leads to  $H_{\text{flop}} = \frac{2}{g\mu_B S} [K(2JS^2 - K)]^{1/2}$ . This result indicates that the spin-flop transition disappears as the MCA energy,  $K$ , approaches zero. Therefore, the thermal evolution of the intrinsic  $K$  can be examined by observing the spin-flop

transition. This often results in peculiar variations in anisotropic magnetic characteristics through phase transformation.

In the plot of the thermally evolved magnetization curve ( $M_c$ ) (Fig. 3a), the small step-like feature at  $H_{\text{flop}}$  and  $T = 2$  K progressively shifts to a lower  $H_c$  and continuously decreases as  $T$  increases to  $T = 30$  K. At  $T = 35$  K, slightly below  $T_N$ ,  $H_{\text{flop}}$  is not observed, which is consistent with previous findings<sup>13,31,36</sup>. Additionally,  $H_{\text{sat}}$  also moves to a lower  $H_c$ , and its shape becomes less pronounced as  $T$  increases. The nonzero slope after  $H_{\text{sat}}$ , which is more evident at higher  $T$ , are attributed to thermal fluctuations inhibiting the saturation of  $M_c$ . In Fig. 3b, the initial magnetization ( $M_b$ ) monotonically increases without any magnetic transition and follows a similar behavior to that of  $H_{\text{sat}}$  for  $M_c$ . The identical shapes of  $M_c$  and  $M_b$  at  $T = 35$  K indicate a magnetically isotropic aspect as the MCA energy fades.

To investigate the decrease in the MCA energy as  $T$  increases, the  $M_c$  in the low  $H_c$  regime was measured for  $T = 30$ – $33$  K (Fig. 3c). Fitting the spin model to the measured  $M_c$  data produces the theoretical  $M_c$ , represented by the dotted curves in Fig. 3c. The feature of  $M_c$  at  $H_{\text{flop}}$ , which is already weakened for  $T = 30$  K, decreases further as  $T$  increases, and  $M_c$  exhibits nearly linear behavior at  $T = 33$  K. This trend is also evident in the  $H_c$  derivative of  $M_c$ , shown in Fig. 3d; here, the peak indicating  $H_c$  is consistently reduced and broadens with a slight increase in  $T$ . The diminished spin-flop transition is more pronounced in the measured and calculated  $H$ -dependent  $\tau$  at  $\theta = -4^\circ$  (Fig. 3e). The broad peak, which results in the occurrence of spin-flops, completely disappeared at  $T = 34$  K.

Fitting the experimental data over the entire  $T$  range leads to an understanding of the impact of thermal softening on  $JS^2$  and the MCA energy. As  $T_N$  is relatively low in CrPS<sub>4</sub>,  $JS^2$  decreases at a relatively slow rate; this shows a decrease of 15.4% at  $T = 33$  K compared to that at  $T = 2$  K (Fig. 3f). Conversely, the MCA energy decreases at a considerably higher rate, with  $K/JS^2$  remaining only at 0.12% at  $T = 33$  K. For a higher  $T$  and reduced antiferromagnetic coupling strength, the Zeeman energy overcomes the coupling strength at lower  $H_c$ , and this contributes to the decline in  $H_{\text{flop}}$ . Additionally, as the MCA energy decreases, the tendency of magnetic moments to align along the easy  $c$ -axis significantly weakens. This leads to an increased angle between two magnetic moments in adjacent layers in the spin-flop state and further diminishes the step-like feature at  $H_{\text{flop}}$ . The increased angle between magnetic moments also shows a reduction in the Zeeman energy that triggers the spin-flop transition; this result is consistent with the shift of  $H_{\text{flop}}$  to lower  $H_c$ . Moreover, approaching the weak limit of MCA energy suppresses the emergence of the spin-flop transition. The theoretical fitting parameters for

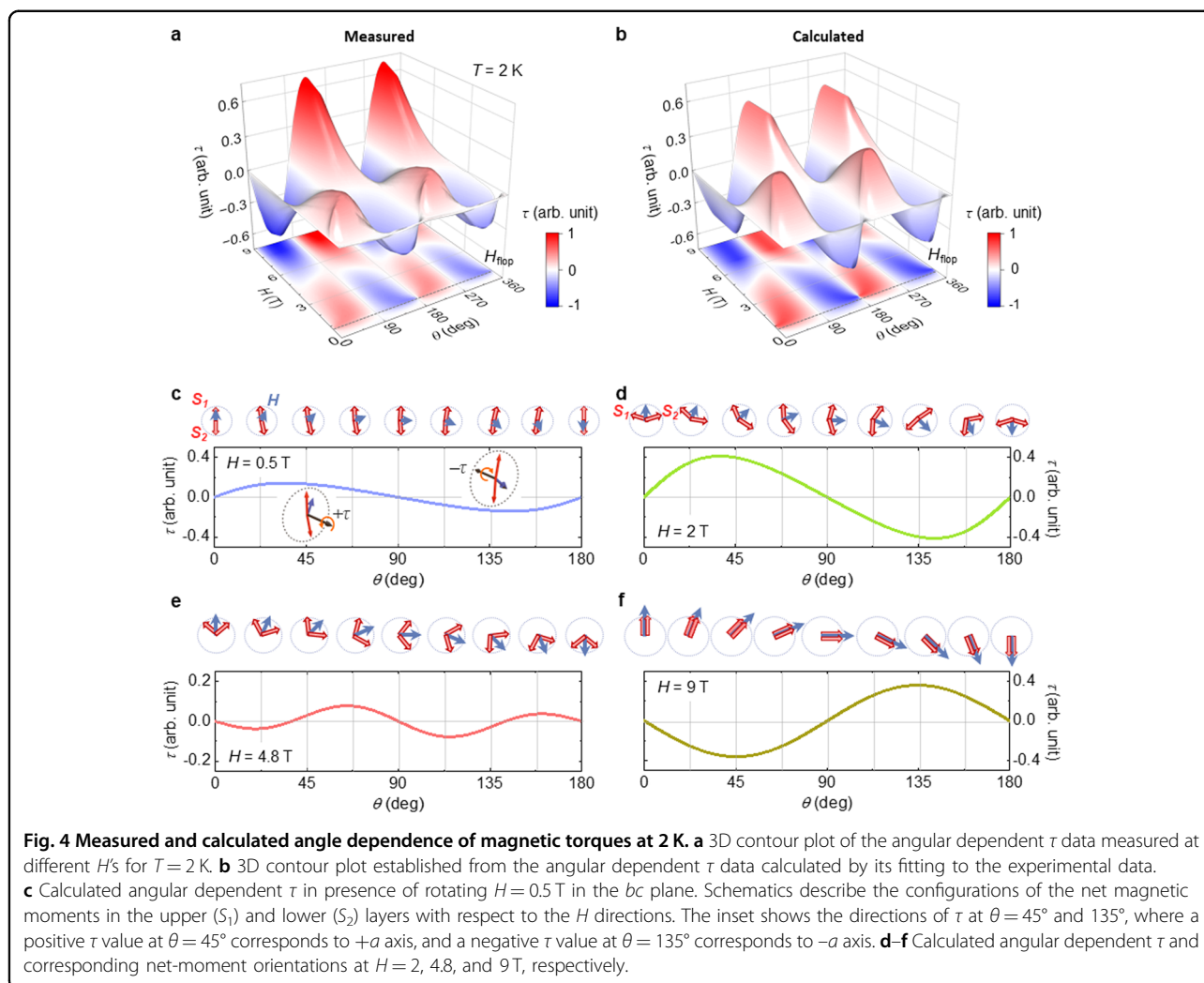


each  $T$  are summarized in Supplementary Table S1. The calculated angles of the  $Cr^{3+}$  spins and the  $M_c$  data for  $T = 2$  K are also listed in Supplementary Table S2.

#### Visualizing spin states directly connected to torque data in rotating magnetic fields

In particular, the  $\tau$  magnetometer has significantly advanced and has enabled accurate measurements of

angular-dependent magnetic characteristics. The occurrence of magnetic  $\tau$  stems from the relative angular disparity between  $M$  and  $H$ , which arises from specific axial anisotropy associated with the MCA. This confirms the suitability of the method for examining the intricate evolution of anisotropic magnetic properties across the spin-flop transition in  $CrPS_4$ . We conducted angle-dependent measurements of  $\tau$  with various  $H$  values at



$T = 2$  K and constructed the 3D contour plots in Fig. 4a; the results reveal a distinct characteristic of  $\tau$  exhibiting a gradual reversal above  $H_{\text{flop}}$ . Furthermore, we performed precise calculations of the minimum total magnetic energy with respect to the uniaxial anisotropic spin Hamiltonian while systematically rotating a specific  $H$ . This further enable the determination of the value of  $\tau$  corresponding to the magnetic moment direction at a given angle. The resulting trend of the  $\tau$  variations closely resembles the experimental outcomes, as shown in Fig. 4b. This reversal behavior observed in angle-dependent  $\tau$  highlights the significant role of the MCA, despite its relatively small magnitude.

Our extensive calculations based on the anisotropic spin model provide a visual representation of the precise orientations of the net  $\text{Cr}^{3+}$  moments during the rotation of  $H$ . These orientations directly correspond to the magnetic torque ( $\tau$ ) data, with theoretically obtained configurations of net magnetic moments in the upper ( $S_1$ ) and lower ( $S_2$ ) layers shown in Fig. 4c–f. The total

magnetization, denoted as  $\mathbf{M} = \mathbf{S}_1 + \mathbf{S}_2$ , resides in the  $bc$  plane with a relative angle to  $\mathbf{H}$ , producing  $\boldsymbol{\tau} = \mathbf{M} \times \mathbf{H}$ . At a weak  $H = 0.5$  T, both the  $S_1$  and  $S_2$  moments exhibit different movements mainly due to the relative orientation of  $H$ , thus yielding a small periodic angle dependence of  $\tau$  (Fig. 4c). For  $\theta$  below  $90^\circ$ , while the  $S_2$  moment turns in the direction of the  $H_b$  component to some extent, the significant AFM exchange interaction causes the  $S_1$  moment to rotate slightly toward a negative angle. Consequently, the resulting value of  $\tau$  is positive mainly because the configuration of the  $S_1$  moment is close to the direction of  $H$ . The sign of  $\tau$  becomes negative for  $\theta > 90^\circ$  because the configuration of the  $S_2$  moment is adjacent to the direction of  $H$ . At  $H = 2$  T, the spin-flop state at  $\theta = 0^\circ$ , where the  $S_1$  and  $S_2$  moments are symmetrically arranged around  $H$ , transforms into another tilted configuration that incorporates the  $S_1$  moment close to the direction of  $H$  as  $\theta$  increases, as shown in Fig. 4d. The impact of the  $H_c$  component on the  $S_1$  moment creates a positive value of  $\tau$  for  $\theta < 90^\circ$ . Although the relative angle

between the net moments and  $H$  becomes slightly smaller, a larger  $H$  generates a more pronounced  $\tau$  signal with positive values. As  $\theta$  crosses  $90^\circ$ , the  $\tau$  state transforms from positive to negative because the alignment of the  $S_1$  moment moves farther away from the direction of  $H$ . With a rotation of  $H = 4.8$  T (Fig. 4e), we observe a partially reversed behavior in  $\tau$  near  $\theta = 0$  and  $180^\circ$ . The slight rotation of  $H$  causes the  $S_2$  moment to move closer to the direction of  $H$ , which aligns with the negative  $\tau$  value observed at  $\theta = 22.5^\circ$ . With further rotation of  $H$ , the  $\tau$  value switches to positive, corresponding to the orientation of the  $S_1$  moment close to  $H$  (the net-moment configuration is shown for  $\theta = 67.5^\circ$ ). Similar variations in the sign of  $\tau$  are repeated, and the sign changes occur twice as frequently with a complete rotation of  $H$ . At  $H = 9$  T, the net moments become fully saturated and move collectively during the rotation of  $H$  (Fig. 4f). However, the orientations of the moments relative to  $H$  are still affected by their preference to align along the magnetic easy  $c$ -axis, leading to a complete reversal of the overall angle dependence of  $\tau$ .

## Discussion

The presence of an axial or planar MCA in an antiferromagnet significantly influences the angular-dependent magnetic  $\tau$  and is suitable for observing the impact of anisotropy on the magnetic properties in vdW magnets. However, such an investigation has yet to be conducted for CrPS<sub>4</sub>. A prior study focused on the  $T$  dependence of isothermal magnetic  $\tau$  on CrPS<sub>4</sub><sup>31</sup>. The analysis in the previous work employed an ordinary conventional phenomenological approach based on the angle derivative of the magnetic free energy, allowing fitting only for the low  $H$  quadratic portion of the isothermal  $\tau$  below the spin-flop field. Therefore, the interpretations were limited by the inherent difficulty in identifying the strength of the MCA and the configurations of relevant spin states. Moreover, validating magnetic  $\tau$  variations through magnetic phase transitions remains limited.

In this comprehensive study, we performed a detailed investigation on the unexplored weak limit of the MCA in the vdW interlayer antiferromagnet CrPS<sub>4</sub>. Based on a combination of magnetic torque measurements and theoretical analysis, we demonstrated the occurrence of a spin-flop transition even at an extremely small anisotropy, providing an essential result for a clear understanding of the magnetic stability at lower dimensionality. This finding is in distinctive contrast to previous research, which primarily focused on increasing the MCA in the vdW magnets to enhance the stability of the magnetic order parameter at higher temperatures or to achieve robust magnetic order down to a monolayer<sup>42–45</sup>.

To explore the intricate spin states in CrPS<sub>4</sub>, we devised an experimental approach based on rotating magnetic

fields, and we complemented this approach with theoretical insights derived from the uniaxial anisotropy spin model. This methodology enables accessing and comprehending the spin directions in each magnetic layer. Notably, conventional experimental tools, such as neutron diffraction and resonant X-ray scattering, have technical challenges in detecting the continuously changing spin states due to limited field geometries. Our advanced approach overcomes this obstacle and provides a constructive means to study the magnetic properties of vdW interlayer antiferromagnets<sup>46–48</sup>.

The versatility of our approach is highlighted by the ability to flexibly modify the anisotropic spin Hamiltonian; thus, our approach is widely applicable for investigating other types of 2D antiferromagnetic materials. By understanding the subtle interactions between the MCA and magnetic order in these materials, we provide the groundwork for further advancements in the field of 2D magnetism. The findings of this study have great potential for the development of spintronic devices and the exploration of novel phenomena in the realm of low-dimensional magnetism.

## Acknowledgements

This work was supported by the National Research Foundation of Korea (NRF) through grants NRF-2021R1A2C1006375, NRF-2022R1A2C1006740, NRF-2022M3K2A108385813, RS-2023-00257561 and RS-2023-00250874. We would like to thank Editage ([www.editage.co.kr](http://www.editage.co.kr)) for English language editing.

## Author contributions

M.K.K., N.L. and Y.J.C. initiated and supervised the project. H.J.S. synthesized the single crystals. J.Y.S., S.L., H.J.S., K.W.J. and J.M.H. performed the measurements of the physical properties. M.K.K. and K.M. performed the theoretical calculations. J.Y.S., M.K.K., K.M., N.L., and Y.J.C. analyzed the data and prepared the manuscript. All authors have read and approved the final version of the manuscript.

## Conflict of interest

The authors declare no competing interests.

## Publisher's note

Springer Nature remains neutral with regard to jurisdictional claims in published maps and institutional affiliations.

**Supplementary information** The online version contains supplementary material available at <https://doi.org/10.1038/s41427-024-00559-3>.

Received: 19 August 2023 Revised: 8 June 2024 Accepted: 13 June 2024  
Published online: 9 August 2024

## References

- Geim, A. K. & Grigorieva, I. V. Van der Waals heterostructures. *Nature* **499**, 419–425 (2013).
- Huang, M. et al. Multifunctional high-performance van der Waals heterostructures. *Nat. Nanotechnol.* **12**, 1148–1154 (2017).
- Burch, K. S., Mandrus, D. & Park, J.-G. Magnetism in two-dimensional van der Waals materials. *Nature* **563**, 47–52 (2018).
- Novoselov, K. S., Mishchenko, A., Carvalho, A. & Castro Neto, A. H. 2D materials and van der Waals heterostructures. *Science* **353**, aac9439 (2016).
- Mak, K. F., Shan, J. & Ralph, D. C. Probing and controlling magnetic states in 2D layered magnetic materials. *Nat. Rev. Phys.* **1**, 646–661 (2019).

6. Gong, C. & Zhang, X. Two-dimensional magnetic crystals and emergent heterostructure devices. *Science* **363**, eaav4450 (2019).
7. Kurebayashi, H., Garcia, J. H., Khan, S., Sinova, J. & Roche, S. Magnetism, symmetry and spin transport in van der Waals layered systems. *Nat. Rev. Phys.* **4**, 150–166 (2022).
8. Gibertini, M., Koperski, M., Morpurgo, A. F. & Novoselov, K. S. Magnetic 2D materials and heterostructures. *Nat. Nanotechnol.* **14**, 408–419 (2019).
9. Song, T. et al. Giant tunneling magnetoresistance in spin-filter van der Waals heterostructures. *Science* **360**, 1214–1218 (2018).
10. Mermin, N. D. & Wagner, H. Absence of ferromagnetism or antiferromagnetism in one-or two-dimensional isotropic Heisenberg models. *Phys. Rev. Lett.* **17**, 1133 (1966).
11. Gong, C. et al. Discovery of intrinsic ferromagnetism in two-dimensional van der Waals crystals. *Nature* **546**, 265–269 (2017).
12. Calder, S. et al. Magnetic structure and exchange interactions in the layered semiconductor CrPS<sub>4</sub>. *Phys. Rev. B* **102**, 024408 (2020).
13. Bud'ko, S. L., Gati, E., Slade, T. J. & Canfield, P. C. Magnetic order in the van der Waals antiferromagnet CrPS<sub>4</sub>: Anisotropic H–T phase diagrams and effects of pressure. *Phys. Rev. B* **103**, 224407 (2021).
14. Huang, B. et al. Layer-dependent ferromagnetism in a van der Waals crystal down to the monolayer limit. *Nature* **546**, 270–273 (2017).
15. Ke, L. & Katsnelson, M. I. Electron correlation effects on exchange interactions and spin excitations in 2D van der Waals materials. *npj Comput. Mater.* **7**, 4 (2021).
16. Fu, H., Liu, C.-X. & Yan, B. Exchange bias and quantum anomalous Hall effect in the MnBi<sub>2</sub>Te<sub>4</sub>/CrI<sub>3</sub> heterostructure. *Sci. Adv.* **6**, eaaz0948 (2020).
17. Sivasdas, N. et al. Stacking-dependent magnetism in bilayer CrI<sub>3</sub>. *Nano Lett.* **18**, 7658–7664 (2018).
18. Fumega, A. O. et al. Electronic structure and magnetic exchange interactions of Cr-based van der Waals ferromagnets. A comparative study between CrBr<sub>3</sub> and Cr<sub>2</sub>Ge<sub>2</sub>Te<sub>6</sub>. *J. Mater. Chem. C* **8**, 13582–13589 (2020).
19. Zhang, G. et al. Above-room-temperature strong intrinsic ferromagnetism in 2D van der Waals Fe<sub>3</sub>GaTe<sub>2</sub> with large perpendicular magnetic anisotropy. *Nat. Commun.* **13**, 5067 (2022).
20. Verzhbitskiy, I. A. et al. Controlling the magnetic anisotropy in Cr<sub>2</sub>Ge<sub>2</sub>Te<sub>6</sub> by electrostatic gating. *Nat. Electron.* **3**, 460–465 (2020).
21. Kriegner, D. et al. Magnetic anisotropy in antiferromagnetic hexagonal MnTe. *Phys. Rev. B* **96**, 214418 (2017).
22. Basnet, R. et al. Highly sensitive spin-flop transition in antiferromagnetic van der Waals material MPS<sub>3</sub> (M= Ni and Mn). *Phys. Rev. Mater.* **5**, 064413 (2021).
23. Nagamiya, T., Yosida, K. & Kubo, R. Antiferromagnetism. *Adv. Phys.* **4**, 1–112 (1955).
24. Jungwirth, T., Marti, X., Wadley, P. & Wunderlich, J. Antiferromagnetic spintronics. *Nat. Nanotechnol.* **11**, 231–241 (2016).
25. Nauman, M. et al. Complete mapping of magnetic anisotropy for prototype Ising van der Waals FePS<sub>3</sub>. *2D Mater.* **8**, 035011 (2021).
26. Shin, H. J. et al. Direct correlation between spin states and magnetic torques in a room-temperature van der Waals antiferromagnet. *NPG Asia Mater.* **15**, 10 (2023).
27. Zhang, M. et al. Spin-Lattice Coupled Metamagnetism in Frustrated van der Waals Magnet CrOCl. *Small* **19**, 2300964 (2023).
28. Basnet, R. et al. Controlling magnetic exchange and anisotropy by non-magnetic ligand substitution in layered MPX<sub>3</sub> (M= Ni, Mn; X= S, Se). *Phys. Rev. Res.* **4**, 023256 (2022).
29. Zhang, Q. et al. Observation of giant optical linear dichroism in a zigzag antiferromagnet FePS<sub>3</sub>. *Nano Lett.* **21**, 6938–6945 (2021).
30. Wildes, A. R. et al. High field magnetization of FePS<sub>3</sub>. *Phys. Rev. B* **101**, 024415 (2020).
31. Peng, Y. et al. Magnetic structure and metamagnetic transitions in the van der Waals antiferromagnet CrPS<sub>4</sub>. *Adv. Mater.* **32**, 2001200 (2020).
32. Lee, M. J. et al. Synaptic devices based on two-dimensional layered single-crystal chromium thiophosphate (CrPS<sub>4</sub>). *NPG Asia Mater.* **10**, 23–30 (2018).
33. Susilo, R. A. et al. Band gap crossover and insulator–metal transition in the compressed layered CrPS<sub>4</sub>. *npj Quantum Mater.* **5**, 58 (2020).
34. Lee, J. et al. Structural and optical properties of single-and few-layer magnetic semiconductor CrPS<sub>4</sub>. *ACS Nano* **11**, 10935–10944 (2017).
35. Son, J. et al. Air-stable and layer-dependent ferromagnetism in atomically thin van der Waals CrPS<sub>4</sub>. *ACS Nano* **15**, 16904–16912 (2021).
36. Peng, Y. et al. Controlling Spin Orientation and Metamagnetic Transitions in Anisotropic van der Waals Antiferromagnet CrPS<sub>4</sub> by Hydrostatic Pressure. *Adv. Funct. Mater.* **32**, 2106592 (2022).
37. Zhuang, H. L. & Zhou, J. Density functional theory study of bulk and single-layer magnetic semiconductor CrPS<sub>4</sub>. *Phys. Rev. B* **94**, 195307 (2016).
38. Tan, L. et al. Spin-flop transition in Gd<sub>2</sub>Ge<sub>4</sub> observed by x-ray resonant magnetic scattering and first-principles calculations of magnetic anisotropy. *Phys. Rev. B* **77**, 064425 (2008).
39. Kimura, S. et al. Submillimetre-wave electron spin-resonance measurements for single-crystal. *J. Phys.: Condens. Matter* **8**, 5461 (1996).
40. Berkowitz, A. & Takano, K. Exchange anisotropy—a review. *J. Magn. Magn. Mater.* **200**, 552–570 (1999).
41. Baltz, V. et al. Antiferromagnetic spintronics. *Rev. Mod. Phys.* **90**, 015005 (2018).
42. Afanasiev, D. et al. Controlling the anisotropy of a van der Waals antiferromagnet with light. *Sci. Adv.* **7**, eabf3096 (2021).
43. Modic, K. A. et al. Robust spin correlations at high magnetic fields in the harmonic honeycomb iridates. *Nat. Commun.* **8**, 180 (2017).
44. Xiao, F. & Tong, Q. Tunable strong magnetic anisotropy in two-dimensional van der Waals antiferromagnets. *Nano Lett.* **22**, 3946–3952 (2022).
45. Li, Z. et al. Magnetic anisotropy control with Curie temperature above 400 K in a van der Waals ferromagnet for spintronic device. *Adv. Mater.* **34**, 2201209 (2022).
46. Pandey, S., Siruguri, V. & Rawat, R. Effect of Tb substitution in naturally layered LaMn<sub>2</sub>Si<sub>2</sub>: magnetic, magnetocaloric, magnetoresistance and neutron diffraction study. *J. Phys.: Condens. Matter* **32**, 035807 (2019).
47. Chen, X. et al. Antiferromagnetic order in Co-doped Fe<sub>3</sub>GeTe<sub>2</sub> probed by resonant magnetic x-ray scattering. *Phys. Rev. Mater.* **6**, 094404 (2022).
48. Pakhira, S. et al. A-type antiferromagnetic order in semiconducting EuMg<sub>2</sub>Sb<sub>2</sub> single crystals. *Phys. Rev. B* **106**, 024418 (2022).